World Scientific
www.worldscientific.com

Intravital imaging of adriamycin-induced renal pathology using two-photon microscopy and optical coherence tomography

Hengchang Guo*, Hsing-Wen Wang*, Qinggong Tang*, Erik Anderson†,
Reuben Falola†, Tikina Smith‡, Yi Liu*, Moshe Levi†,
Peter M. Andrews† and Yu Chen*,§

*Fischell Department of Bioengineering
University of Maryland
College Park, MD 20742, USA

†Department of Biochemistry and Molecular & Cellular Biology
Georgetown University Medical Center
Washington DC 20007, USA

‡Central Animal Resources Facility
University of Maryland, College Park, MD 20742, USA
§yuchen@umd.edu

Adriamycin (doxorubicin), a common cancer chemotherapeutic drug, can be used to induce a model of chronic progressive glomerular disease in rodents. In our studies, we evaluated renal changes in a rat model after Adriamycin injection using two-photon microscopy (TPM), optical coherence tomography (OCT) and Doppler OCT (DOCT). Taking advantage of deep penetration and fast scanning speed for three-dimensional (3D) label-free imaging, OCT/DOCT system was able to reveal glomerular and tubular pathology noninvasively and in real time. By imaging renal pathology following the infusion of fluorophore-labeled dextrans of different molecular weights, TPM can provide direct views of glomerular and tubular flow dynamics with the onset and progression of renal disease. Specifically, glomerular permeability and filtration, proximal and distal tubular flow dynamics can be revealed. 6–8 weeks after injection of Adriamycin, TPM and OCT/DOCT imaging revealed glomerular sclerosis, compromised flow across the glomerular wall, tubular atrophy, tubular dilation, and variable intra-tubular flow dynamics. Our results indicate that TPM and OCT/DOCT provide real-time imaging of renal pathology *in vivo* that has not been previously available using conventional microscopic procedures.

§Corresponding author.

1. Introduction

Chronic kidney disease (CKD) is a growing health problem among the aging population.[1–5] It associates with a decline in renal function characterized pathologically by reduced glomerular filtration rate (GFR), glomerulosclerosis, interstitial fibrosis and tubular atrophy/dilation.[1,2,4,6] Adriamycin (doxorubicin) has been used to induce a model of CKD in rodents producing results similar to human CKD.[7,8]

Kidney disease has been monitored using a number of different imaging modalities, including ultrasound, computed tomography (CT) and magnetic resonance imaging (MRI).[5,9] Although these techniques allow for noninvasive, deep penetration and wide field-of-view imaging, they do not have sufficient resolution to detect changes in renal microcirculation and pathology associated with microanatomy. Optical imaging techniques that have higher resolutions and greater sensitivities will provide more information for functional/structural correlations of pathological events in the kidney.[10–16] Studies using confocal microscopy[17,18] have demonstrated the ability to image kidney microstructure on animal models with high-resolution and fluorescence detection capability, but the penetration depth has been limited to a few hundred microns. Two-photon microscopy (TPM) is a rapidly emerging technology for high-resolution fluorescence molecular imaging and intravital studies.[14,19–30] TPM has been used for kidney function studies to image blood flow, glomerular filtration and permeability, tubular flow dynamics and tubular re-absorption.[14–16,31–33]

Optical coherence tomography (OCT) is another established biophotonic imaging technology, which has been developed for subsurface imaging of tissues with high resolution ($<10\,\mu$m) and 1–2 mm penetration depth.[34–38] The performance of OCT is comparable to that of the standard pinch biopsy and histology. OCT has the capability of generating high-resolution cross-sectional images of tissue morphology *in situ* and in real time.[34,39,40] Its functional extension Doppler OCT (DOCT) has been shown to visualize blood flow noninvasively by measuring Doppler frequency shifts in the OCT interference signal caused by moving scatters (i.e., red blood cells).[10–13,41–43] More recently, a novel OCT-based technique for label-free 3D imaging of blood circulations *in vivo*, termed optical microangiography (OMAG), has been developed rapidly.[44,45]

In the study, we use TPM and OCT/DOCT for kidney function imaging on an Adriamycin-induced murine model of CKD. Our objective is to demonstrate the feasibility of using noninvasive intravital imaging techniques TPM/OCT to observe renal function within living kidneys in real time and evaluate the onset and progression of CKD,[46–51] and compare the characteristics of each modality. TPM and OCT/DOCT imaging reveal tubular atrophy, tubular distention, and glomerular sclerosis in the distal nephron over the 4–8 weeks after injection. Our studies indicate that combining TPM and OCT/DOCT can be a valuable procedure for evaluating renal histopathology.

2. Materials and Methods

2.1. *Animal models and procedures*

The animal protocol has been approved by the committee on animal care and use at the University of Maryland College Park. Adult male Munich-Wistar rats were used in this study. This strain of rats has numerous superficial glomeruli in the outer cortex[52] that are accessible for TPM and OCT observations. The rats were maintained on a standard Purina Rat Chow diet (Ralston Purina Co., St Louis, MO, USA) and *ad lib* water intake. All rats had normal kidney function as determined by analyses of serum creatinine (less than or equal to 1.3 mg/dl), urine volume and urine protein. Urine volume was collected with metabolic cages. Urine protein was tested with testing stick. Serum creatinine was measured using creatinine analyzer (Creatinine Analyzer, Beckman Coulter, CA, USA).

Forty rats were imaged in this study and they were regularly fed with normal rat chow with free access to water at all times. Eight rats served as control rats and 32 rats were injected with Adriamycin (1.5 mg/kg). Adriamycin is a chemotherapy drug, which will speedily induce renal injury due to primary focal segmental glomerulosclerosis.[46] Once a week during the 8 week study protocol, five rats

(one control and 4 rats injected with Adriamycin) were weighed and 24 h urine volumes were collected in metabolic cages. At the day of imaging, fresh urine samples were tested for albuminuria (Albustix, Leverkusen, Germany), and blood samples taken from the tail vein were analyzed for serum creatinine (Creatinine Analyzer, Beckman Coulter, CA, USA). Prior to surgery, the animals were anesthetized with isoflurane/O2 (isoflurane: 4% induction and 1.5% during operation; O2: 1 L/min) and monitored routinely by tactile stimulation with supplemental anesthetic added as needed to maintain initial depth of anesthesia. After induction of anesthesia, the abdominal cavity was opened through a midline incision, and the left kidney exposed and studied using TPM and OCT for *in vivo* imaging. Multiple images from different locations were acquired. Immediately following imaging, the kidneys were fixed *in situ* by flushing with warm (i.e., 37°C) oxygenated saline, followed immediately by phosphate buffered 2% paraformaldehyde and 0.1% glutaraldehyde. The fixed kidneys were excised and the rat was euthanized by intracardiac injection of pentobarbital sodium to induce cardiac arrest. Blocks of fixed kidneys were embedded in paraffin, sectioned, stained with hematoxylin and eosin (H&E), and then examined and photographed with a light microscope (BH-2, Olympus, Center Valley, PA).

2.2. *OCT and DOCT*

A high-speed, high-resolution Fourier-domain OCT system was used in this study.[10,13,53–55] The details of the OCT system have been previously described.[13] Briefly, an OCT system consisting of a swept-source laser (100 nm bandwidth at 1310 nm center wavelength) yielding an axial resolution of 10 μm in tissue was used. A 10x objective (Olympus Plan N, NA = 0.25) was used in the sample arm to achieve a lateral resolution of 5–6 μm determined by a USAF resolution target. The laser source operated at a sweep rate of 16 kHz, allowing a series of two-dimensional cross-sectional images to be captured in real time to form a three-dimensional (3D) data set (voxel size: 1024 [X] by 256 [Y] by 512 [Z] pixels; dimension: 1.4 mm [X] by 0.325 mm [Y] by 1.90 mm [Z]; acquisition time 20 s). OCT interference data were acquired to obtain both amplitude and phase information after Fourier transform, and DOCT

signals were computed using standard phased-resolved algorithm.[56] Glomeruli were first located by scanning the surface of the renal cortex, and 3D data sets were acquired for each glomerulus. OCT intensity images as well as DOCT images were computed from the interference data for each frame in the 3D data sets. Quantification of single glomerular microcirculation parameters was performed offline using a custom image analysis program written in Matlab (Mathworks, Natick, MA, USA).

2.3. *Two-photon microscopy (TPM)*

TPM images were acquired using a nonlinear optical imaging system based on a custom-built multiphoton microscope and a Ti:Sapphire laser (Mira 900-F, Coherent, Santa Clara, CA, USA) operating at 790 nm wavelength and 120 fs pulse width.[57,58] A silicon oil immersion objective (Olympus 60x, NA = 1.3) was employed for focusing the excitation beam into tissue samples and was also used to collect the backscattered intrinsic two-photon excited fluorescence signals. The working distance of the 60x objective limits the imaging depth to 300 μm into kidney tissues. For Munich-Wistar rats, this distance is sufficient to image superficial glomeruli, proximal and distal tubules in intact kidneys. Fluorescent dyes were dissolved in 1.0 ml sterile isotonic saline solution and intravenously injected into rats. Hoechst 33342 was used for nuclei labeling (2 mg/ml). Large molecule-weight (MW) 500-kDa dextran-Fluorescein (5 mg/ml) was used for the visualization of blood flow, as well as glomerulus filtration and permeability. Since large MW dextran is not filtered by normal glomerulus and remains in the vasculature, it labels the peritubular and glomerular capillaries. Small MW 10-kDa dextran-Rhodamine (2.5 mg/ml) was used for the observation of glomerulus filtration, as well as visualization of proximal and distal tubules. All dyes were obtained from Molecular Probes (Grand Island, NY).

3. Results

From the previous data, the normal sizes of the proximal and distal tubules are around 25–40 μm.[12,59] The normal sizes of glomerular and Bowman's space are around 97.40 ± 19.02 μm and 6.18 ± 1.49 μm, respectively.[60] In the first 3 weeks after Adriamycin injection, OCT reveals open
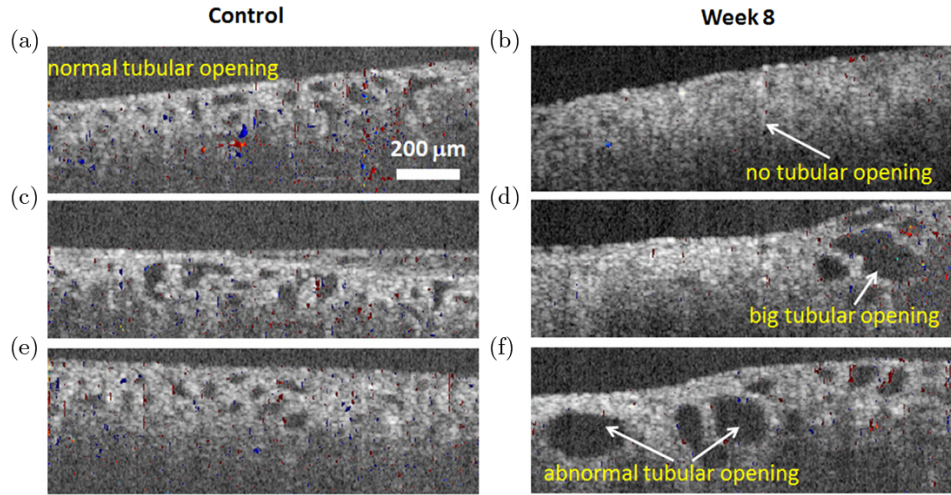
Fig. 1. OCT/DOCT imaging shows the tubules in rat kidneys. Cross-sectional OCT/DOCT images of normal (a) and diseased rat kidneys after Adriamycin (Doxorubicin) induced CKD at week 2 (c) ,week 3 (e), week 8 (b,d,f). Less blood flow inside glomeruli was seen at weeks 2 and 3 after drug induction (c, e).

lumens of uriniferous tubules (mainly proximal convoluted tubules) that appeared rounded in cross-sectional profile, with a mean diameter less than $50\,\mu$m (Figs. 1(a), 1(c), 1(e)). In rat kidneys 6–8 week post-injection, OCT shows closed lumens and dilated uriniferous tubules with diameter up to $200\,\mu$m (Figs. 1(b), 1(d), 1(f)). Figure 2 shows representative TPM auto-fluorescence imaging of kidney morphology. Figure 2(a) shows control kidney with normal proximal and distal tubules. Figures 2(b) and 2(c) show CKD kidney 8 weeks after Adriamycin injection. Dilated tubules (Fig. 2(b)) and atrophic tubules (Fig. 2(c)) were found from these high-resolution fluorescence images. The foregoing OCT/TPM observations are verified by light microscopic examination of the same samples using conventional H&E staining. The control rat kidney shows normal appearance of the uriniferous tubules (Fig. 3(a)), while the CKD rat kidney shows

dilated tubules and regions of interstitial fibrosis (Fig. 3(b)).

Figure 4 shows cross-sectional OCT/DOCT images revealing renal microanatomy and the spatial location of the DOCT signal within the glomerulus. The upper row images are from a control rat kidney and the bottom row images are from a CKD rat kidney 8 weeks following Adriamycin injection. Sclerotic glomeruli are visualized and distinguished from normal by the irregularly distended Bowman's space volume and shrunken capillary tuft (bottom row images). OCT can visualize the shrinkage of the sclerotic glomerular capillary tufts. The corresponding DOCT images from the same plane depict reduced blood flow (i.e., fewer red/blue color pixels in the bottom row images).

Healthy kidneys remove wastes and extra water in the body. As blood flows into each nephron, it enters a cluster of tiny blood vessels, which is the
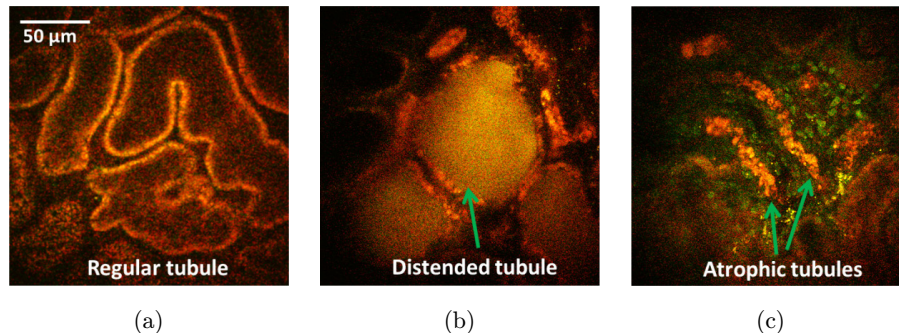

Fig. 2. TPM imaging of regular tubules from control model (a) distended tubules (b) and atrophic tubules (c) induced by CKD.
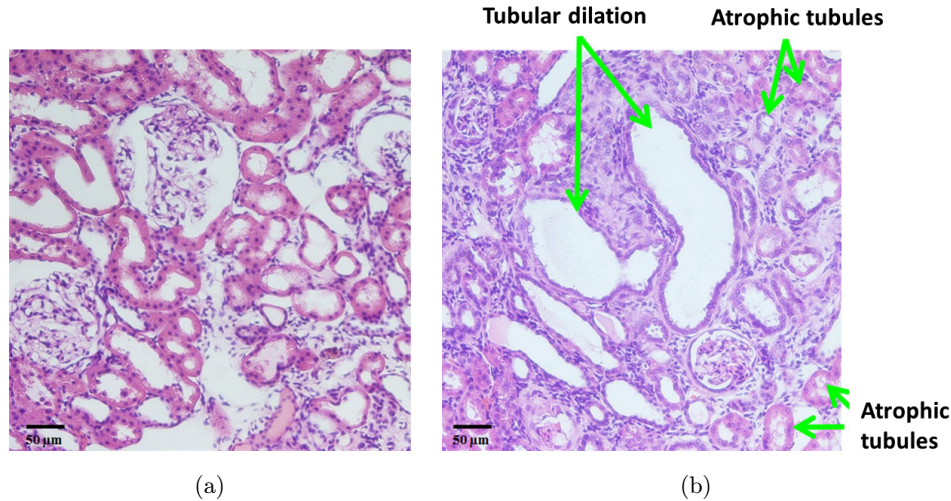
Fig. 3. Histology images with H&E staining (a) Normal tubules show regular size and opening, (b) CKD rat show distended tubules and atrophic tubules.
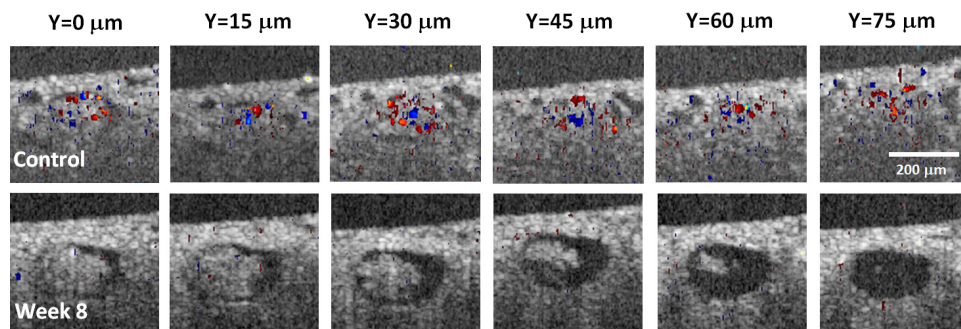

Fig. 4. Increased Bowman's space and decreased blood flow were seen in the glomerulus of week 8 CDK animal, indicating glomerulosclerosis. Numbers on the top indicated different cross-sections across a single glomerulus.

glomerulus. The smaller molecules, wastes and fluid are able to pass the thin walls of the glomerulus into the tubule, while larger molecules, such as proteins and blood cells, stay in the blood vessel.[61]

Molecules traversing the filtration barrier called the extracellular slit diaphragm in the glomerulus are selected according to their size, shape and charge.[62,63] Previous data have shown that the slit diaphragm forms the ultimate barrier for macromolecular permeability.[64–66] The slit pore size was reported to be a rectangular pore approximately 3.5–4 nm by 14 nm in cross-section and 7 nm in length in rat.[62,67] The molecular sizes of the labeling fluorophores can be estimated from the equation $R_{\min} = 0.066\,M^{1/3}$, where M is the MW in Dalton and $R_{\min}$ is the radius in nm.[68] The molecular radii of 10-kDa dextran-Rhodamine and 500-kDa dextran-fluorescein are around 1.4 nm and 5.2 nm, respectively. Based on the sizes, we chose 10-kDa dextran-Rhodamine and 500-kDa dextran-fluorescein for the observation of glomerulus permeability and filtration differences in normal and CKD rats. 500-kDa dextran-Fluorescein was used in TPM for the visualization of blood flow as shown in Video 1. Figure 5 shows the normal filtration in control animal [upper row, Video 2] and the abnormal CKD model [bottom row, Video 3]. Each row shows time series of images at 0 s (injection of 10-kDa Dextran-Rhodamine), 2 s, 4 s and 2 min. Slower blood flow and permeability in the CKD model indicates glomerulosclerosis. Also the CKD rat kidney shows selective filtration across specific regions of the glomerular wall. Corresponding histology (Fig. 6) shows a good correlation of the anatomic features observed by OCT/TPM with conventional H&E stained light microscopic images. Figure 6(a) shows normal glomeruli including capillaries and Bowman's space. Figure 6(b) reveals
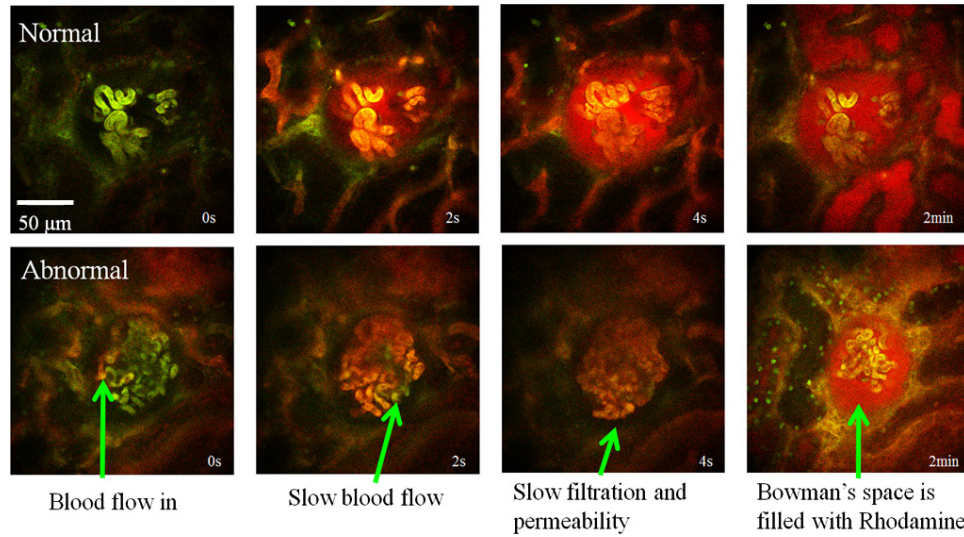
Fig. 5. TPM imaging shows the normal filtration in control animal [upper row,Video2] and abnormal CKD model [bottom row, Video3]. Each row shows time series of images at 0 s (injection of 10-kDa Dextran-Rhodamine), 2 s, 4 s, and 2 min. Slow blood flow and permeability in the CKD model indicating glomerulosclerosis (Video2, QuickTime, 25.2 MB; Video2, QuickTime, 12.2 MB).
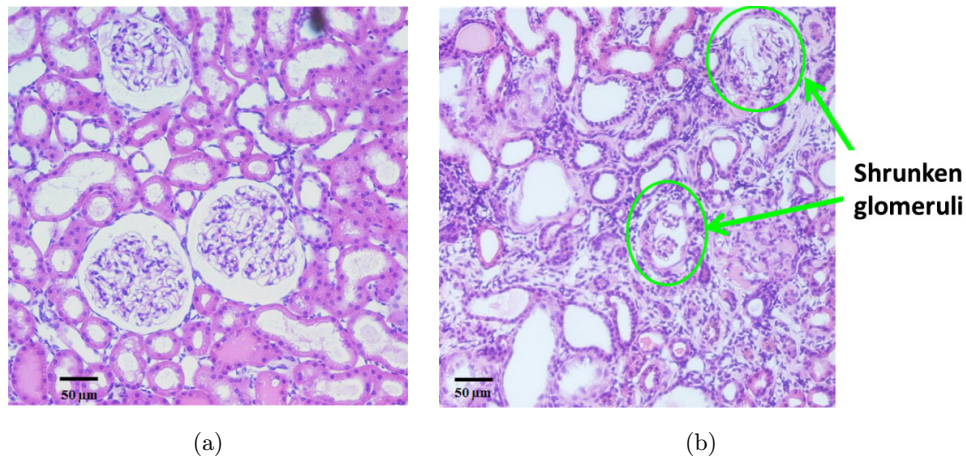
Fig. 6. Histology images with H&E staining (a) Normal glomeruli shows capillaries and Bowman's space, (b) Glomerulosclerosis show glomerular degeneration and shrunken glomeruli (arrows).
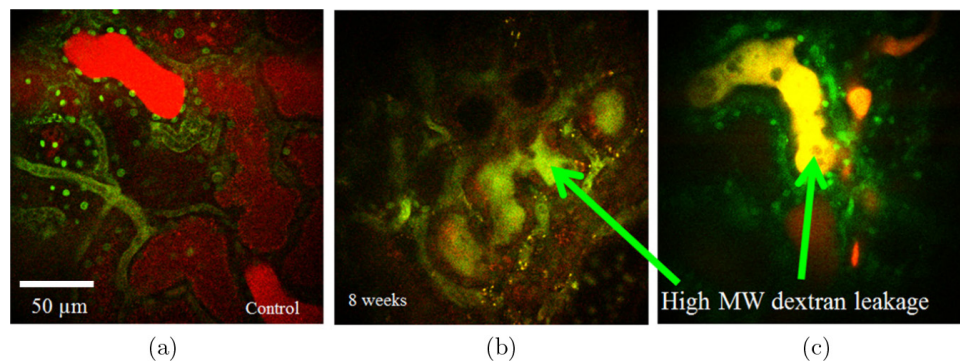

Fig. 7. TPM imaging of dextrans filtration from glomeruli (a) Small molecule weight (MW) 10-kDa dextran-Rhodamine was detected in proximal and distal tubules. In CKD model, injury of podocytes induced the leakage of high MW 500-kDa dextran-Fluorescein into tubules (b, c).

glomerulosclerosis with glomerular degeneration and shrunken glomeruli.

TPM can also visualize glomerular permeability and tubular flow dynamics in normal and CKD rats. Figure 7 shows TPM imaging of dextrans in tubules after filtration from glomeruli. In normal kidney, small MW 10-kDa dextran-Rhodamine was detected in both proximal and distal tubules, but no large MW 500-kDa dextran-Fluorescein was seen, as shown in Fig. 7(a). In CKD model, injury of podocytes induced the leakage of high MW 500-kDa dextran-Fluorescein into tubules, as shown by the yellow color (mixture of red and green) in Figs. 7(b) and 7(c).

4. Discussion

Due to the highly inhomogeneous and light-scattering structure of living renal tissue, the application of conventional imaging techniques is more difficult compared with other parenchymal organs.[69] Moreover, key physiological processes of the kidney, such as glomerular filtration and hemodynamics, involve complex interactions between multiple cell types which might require more advanced imaging methods with improved resolution, imaging speed and penetration depth.[69] TPM offers many advantages over conventional imaging techniques and is superior for deep optical sectioning of living tissue samples.[14,16,20,21,27,57,69,70] Dynamic regulatory processes and multiple functions in the intact kidney have been visualized using TPM in real time, noninvasively, and with submicron resolution.[71–73] The process of glomerular filtration has been visualized with high temporal resolution by using water-soluble, freely filtered, low-molecular-weight fluorescent markers,[14,32,33,74] which allows the calculation of single nephron glomerular filtration rate (SNGFR).[32] OCT and DOCT (or optical Doppler tomography, ODT) enable depth-resolved high-resolution tomographic imaging of tissue microstructure and blood flow.[41,43] Thus, OCT/DOCT represent a powerful tool to evaluate kidney status *in vivo* and in real time and have been demonstrated in imaging living human kidney.[10,11,75]

In this paper, we applied TPM and OCT/DOCT to evaluate kidney microstructures and associated renal function in a murine CKD model induced by Adriamycin at different time points *in vivo* and *in situ*. Over time, the rats exhibited a decrease in body weight, proteinuria, polyuria, and a rise in serum creatinine values. Both TPM and OCT are able to delineate the morphological architectures of normal rat kidney and CKD kidney. OCT provides larger field-of-view to locate glomerulosclerosis and abnormal tubules, but with lower resolution. TPM has smaller field-of-view but higher resolution, and has the unique capability of fluorescence imaging. OCT reveals dilated tubules, regions of tubular degeneration, and associated interstitial fibrosis at later stage (week 6–8). Finally, many of the glomeruli appeared shrunken and sclerotic. DOCT shows that there are less visible capillary tufts with distended Bowman's space in CKD rat kidney, which is difficult to obtain using conventional medical imaging modalities. Conventional light microscopy confirms same histopathological features, including dilated tubules, interstitial fibrosis, degenerating tubules, as well as sclerotic glomeruli. TPM reveals additional detailed images of tubular flow and glomerular permeability and filtration. Another observation is the decreased blood flow and permeability in the CKD model. The small MW dextran also shows selective filtration across specific regions of the glomerular wall in the CKD model. The combined use of TPM and OCT imaging techniques provides more comprehensive diagnostic information that cannot be obtained from conventional kidney function measurement such as blood creatinine and urine volume.

In addition, TPM/OCT images may further provide: (1) morphological/structural parameters indicating tubular atrophy, glomerulosclerosis, and interstitial fibrosis; (2) functional parameters indicating renal hemodynamics and glomerular filtration rate (GFR). Specifically, we have quantified tubular atrophy/hypertrophy during CKD progression using a fully automated computer-vision algorithm based on machine learning.[59] Future development in computer-aided diagnosis (CAD) methods might enable the quantification of glomerulosclerosis and interstitial fibrosis from OCT images, hemodynamics from DOCT images, and glomerular permeability from TPM images.

5. Summary

Our results demonstrate the strong potential and promise for the application of TPM and OCT/DOCT in imaging kidney pathology, as it provides a more comprehensive real-time examination of renal pathology. These techniques have the potential to

become a powerful tool for functional optical renal biopsy in the future.

Conflict of Interest

The authors declare no competing financial interests.

Acknowledgments

References

1. A. S. Go, G. M. Chertow, D. J. Fan, C. E. McCulloch, C. Y. Hsu, "Chronic kidney disease and the risks of death, cardiovascular events, and hospitalization," *N. Engl. J. Med.* **351**, 1296–1305 (2004).

2. A. S. Levey *et al.*, "National kidney foundation practice guidelines for chronic kidney disease: Evaluation, classification, and stratification," *Ann. Int. Med.* **139**, 137–147 (2003).

3. R. J. Glassock, D. G. Oreopoulos, "Aging and chronic kidney disease," *Nephron Clin. Pract.* **119**, c1–c1 (2011).

4. M. Tonelli *et al.*, "Chronic kidney disease and mortality risk: A systematic review," *J. Am. Soc. Nephrol.* **17**, 2034–2047 (2006).

5. A. S. Levey, J. Coresh, "Chronic kidney disease," *The lancet* **379**, 165–180 (2012).

6. A. S. Levey *et al.*, "Definition and classification of chronic kidney disease: A position statement from Kidney Disease: Improving Global Outcomes (KDIGO)," *Kidney Int.* **67**, 2089–2100 (2005).

7. A. Chen *et al.*, "Experimental focal segmental glomerulosclerosis in mice," *Nephron* **78**, 440–452 (1998).

8. E. Bucciarelli, R. Binazzi, P. Santori, G. Vespasiani, "Nephrotic syndrome in rats due to adriamycin chlorhydrate," *Lav. Ist. Anat. Istol. Patol. Univ. Studi Perugia* **36**, 52–69 (1976).

9. J. J. Nikken, G. P. Krestin, "MRI of the kidney-state of the art," *Eur. Radiol.* **17**, 2780–2793 (2007).

10. P. Andrews *et al.*, "Optical coherence tomography of the living human kidney," *J. Innov. Opt. Health Sci.* **7**, 1350064 (2014).

11. P. M. Andrews *et al.*, "High-resolution optical coherence tomography imaging of the living kidney," *Lab. Invest.* **88**, 441–449 (2008).

12. Y. Chen, P. M. Andrews, A. D. Aguirre, J. M. Schmitt, J. G. Fujimoto, "High-resolution three-dimensional optical coherence tomography imaging of kidney microanatomy *ex vivo*," *J. Biomed. Opt.* **12**, 034008 (2007).

13. J. Wierwille *et al.*, "*In vivo*, label-free, three-dimensional quantitative imaging of kidney microcirculation using Doppler optical coherence tomography," *Lab. Invest.* **91**, 1596–1604 (2011).

14. K. W. Dunn *et al.*, "Functional studies of the kidney of living animals using multicolor two-photon microscopy," *Am. J. Physiol. Cell Physiol.* **283**, C905–C916 (2002).

15. S. L. Ashworth, R. M. Sandoval, G. A. Tanner, B. A. Molitoris, "Two-photon microscopy: Visualization of kidney dynamics," *Kidney Int.* **72**, 416–421 (2007).

16. C. L. Phillips *et al.*, "Three-dimensional imaging of embryonic mouse kidney by two-photon microscopy," *Am. J. Pathol.* **158**, 49–55 (2001).

17. P. M. Andrews, W. M. Petroll, H. D. Cavanagh, J. V. Jester, "Tandem Scanning Confocal Microscopy (Tscm) of normal and ischemic living kidneys," *Am. J. Anat.* **191**, 95–102 (1991).

18. P. M. Andrews, B. S. Khirabadi, B. C. Bengs, "Using tandem scanning confocal microscopy to predict the status of donor kidneys," *Nephron* **91**, 148–155 (2002).

19. S. Quentmeier, S. Denicke, K. H. Gericke, "Two-color two-photon fluorescence laser scanning microscopy," *J. Fluores.* **19**, 1037–1043 (2009).

20. P. T. C. So, H. Kim, I. E. Kochevar, "Two-photon deep tissue ex vivo imaging of mouse dermal and subcutaneous structures," *Opt. Express* **3**, 339–350 (1998).

21. W. Denk, J. H. Strickler, W. W. Webb, "Two-photon laser scanning fluorescence microscopy," *Science* **248**, 73–6 (1990).

22. H. C. Guo *et al.*, "Two-photon fluorescence imaging of intracellular hydrogen peroxide with chemoselective fluorescent probes," *J. Biomed. Opt.* **18**, 106002 (2013).

23. W. R. Zipfel, R. M. Williams, W. W. Webb, "Nonlinear magic: Multiphoton microscopy in the biosciences," *Nature Biotechnol.* **21**, 1368–1376 (2003).

24. Y. Chen *et al.*, "Recent advances in two-photon imaging: Technology developments and biomedical applications," *Chin. Opt. Lett.* **11**, 011703 (2013).

25. G. McConnell, E. Riis, "Two-photon laser scanning fluorescence microscopy using photonic crystal fiber," *J. Biomed. Opt.* **9**, 922–927 (2004).

26. F. Helmchen, W. Denk, "Deep tissue two-photon microscopy," *Nature Meth.* **2**, 932–940 (2005).

27. E. M. C. Hillman *et al.*, "Depth-resolved optical imaging and microscopy of vascular compartment dynamics during somatosensory stimulation," *Neuroimage* **35**, 89–104 (2007).

28. M. B. Ericson *et al.*, "Two-photon laser-scanning fluorescence microscopy applied for studies of human skin," *J. Biophotonics* **1**, 320–330 (2008).

29. D. G. Ouzounov *et al.*, "*In vivo* three-photon imaging of activity of GCaMP6-labeled neurons deep in intact mouse brain," *Nature meth.* **14**, 388–390 (2017).

30. W. Liang, G. Hall, B. Messerschmidt, M.-J. Li, X. Li, "Nonlinear optical endomicroscopy for label-free functional histology *in vivo*," *Light: Science & Applications* **6**, e17082 (2017). DOI: 10.1038/lsa.2017.82.

31. H. Koepsell, "*In vivo* two-photon fluorescence microscopy opens a new area for investigation of the excretion of cationic drugs in the kidney," *Kidney Int.* **72**, 387–388 (2007).

32. J. J. Kang, I. Toma, A. Sipos, F. McCulloch, J. Peti-Peterdi, "Quantitative imaging of basic functions in renal (patho)physiology," *Am. J. Physiol. Renal Physiol.* **291**, F495–F502 (2006).

33. B. A. Molitoris, R. M. Sandoval, "Intravital multiphoton microscopy of dynamic renal processes," *Am. J. Physiol. Renal Physiol.* **288**, F1084–F1089 (2005).

34. D. Huang *et al.*, "Optical coherence tomography," *Science* **254**, 1178–81 (1991).

35. J. G. Fujimoto *et al.*, "Optical biopsy and imaging using optical coherence tomography," *Nature Med.* **1**, 970–972 (1995).

36. G. J. Tearney *et al.*, "*In vivo* endoscopic optical biopsy with optical coherence tomography," *Science* **276**, 2037–2039 (1997).

37. B. E. Bouma, S. H. Yun, B. J. Vakoc, M. J. Suter, G. J. Tearney, "Fourier-domain optical coherence tomography: Recent advances toward clinical utility," *Curr. Opin. Biotechnol.* **20**, 111–118 (2009).

38. C. Kut *et al.*, "Detection of human brain cancer infiltration ex vivo and in vivo using quantitative optical coherence tomography," *Sci. Trans. Med.* **7**, 292ra100 (2015).

39. J. G. Fujimoto, C. Pitris, S. A. Boppart, M. E. Brezinski, "Optical coherence tomography: An emerging technology for biomedical imaging and optical biopsy," *Neoplasia* **2**, 9–25 (2000).

40. J. G. Fujimoto, "Optical coherence tomography for ultrahigh resolution in vivo imaging," *Nat. Biotechnol.* **21**, 1361–1367 (2003).

41. Z. P. Chen *et al.*, "Noninvasive imaging of in vivo blood flow velocity using optical Doppler tomography," *Opt. Lett.* **22**, 1119–1121 (1997).

42. J. A. Izatt, M. D. Kulkarni, S. Yazdanfar, J. K. Barton, A. J. Welch, "*In vivo* bidirectional color Doppler flow imaging of picoliter blood volumes using optical coherence tomograghy," *Opt. Lett.* **22**, 1439–1441 (1997).

43. Y. H. Zhao *et al.*, "Doppler standard deviation imaging for clinical monitoring of in vivo human skin blood flow," *Opt. Lett.* **25**, 1358–1360 (2000).

44. R. K. Wang, "Optical microangiography: A label-free 3-D imaging technology to visualize and quantify blood circulations within tissue beds *in vivo*," *IEEE J. Sel. Top. Quantum Electron.* **16**, 545–554 (2010).

45. Q. Zhang *et al.*, "Wide-field optical coherence tomography based microangiography for retinal imaging," *Sci. Rep.* **6**, 22017 (2016).

46. V. W. S. Lee, D. C. H. Harris, "Adriamycin nephropathy: A model of focal segmental glomerulosclerosis," *Nephrology* **16**, 30–38 (2011).

47. J. W. Pippin *et al.*, "Inducible rodent models of acquired podocyte diseases," *Am. J. Physiol. Renal Physiol.* **296**, F213–F229 (2009).

48. T. Bertani *et al.*, "Adriamycin-induced nephrotic syndrome in rats — sequence of pathologic events," *Lab. Invest.* **46**, 16–23 (1982).

49. T. Bertani, F. Cutillo, C. Zoja, M. Broggini, G. Remuzzi, "Tubulointerstitial lesions mediate renal damage in adriamycin glomerulopathy," *Kidney Int.* **30**, 488–496 (1986).

50. J. Grond, J. J. Weening, J. D. Elema, "Glomerular sclerosis in nephrotic rats — comparison of the long-term effects of adriamycin and aminonucleoside," *Lab. Invest.* **51**, 277–285 (1984).

51. S. Okuda *et al.*, "Adriamycin-induced nephropathy as a model of chronic progressive glomerular-disease," *Kidney Int.* **29**, 502–510 (1986).

52. H. Hackbarth *et al.*, "Distribution of glomeruli in the renal cortex of munich wistar fromter (Mwf) rats," *Renal Physiol. Biochem.* **6**, 63–71 (1983).

53. Q. Tang *et al.*, "Depth-resolved imaging of colon tumor using optical coherence tomography and fluorescence laminar optical tomography," *Biomed. Opt. Exp.* **7**, 5218–5232 (2016).

54. Q. Tang, C.-P. Liang, K. Wu, A. Sandler, Y. Chen, "Real-time epidural anesthesia guidance using optical coherence tomography needle probe," *Quant. Imag. Med. Surg.* **5**, 118–124 (2014).

55. Q. Tang *et al.*, "High-dynamic-range fluorescence laminar optical tomography (HDR-FLOT)," *Biomed. Opt. Exp.* **8**, 2124–2137 (2017).

56. V. X. Yang *et al.*, "High speed, wide velocity dynamic range Doppler optical coherence tomography (Part III): *In vivo* endoscopic imaging of blood flow in the rat and human gastrointestinal tracts," *Opt. Exp.* **11**, 2416–2424 (2003).

57. Q. Tang *et al.*, "Real-time monitoring of microdistribution of antibody-photon absorber conjugates

during photoimmunotherapy *in vivo*," *J. Control. Release* **260**, 154–163 (2017).

58. Z. Ding *et al.*, "*In Oxygen transport to tissue XXXVIII*," (Eds. Q. Luo, L. Z. Li, D. K. Harrison, H. Shi, D. F. Bruley) 345–350, Springer International Publishing, Cham, (2016).

59. H.-W. W. Bohan Wang, H. Guo, E. Anderson, Q. Tang, P. M. Andrews, Y. Chen, "Optical Coherence Tomography (OCT) and Computer-Aided Diagnosis (CAD) of a murine model of Chronic Kidney Disease (CKD)," *J. Biomed. Opt.* **22**, 121706 (2017). DOI: 10.1117/1.JBO.22.12.121706.

60. T. Kotyk *et al.*, "Measurement of glomerulus diameter and Bowman's space width of renal albino rats," *Comput. Meth. Program. Biomed.* **126**, 143–153 (2016).

61. https://www.niddk.nih.gov/health-information/kidney-disease/kidneys-how-they-work.

62. J. Wartiovaara *et al.*, "Nephrin strands contribute to a porous slit diaphragm scaffold as revealed by electron tomography," *J. Clin. Invest.* **114**, 1475–1483 (2004).

63. Y. S. Kanwar, Z. Z. Liu, N. Kashihara, E. I. Wallner, "Current status of the structural and functional basis of glomerular filtration and proteinuria," *Semin. Nephrol.* **11**, 390–413 (1991).

64. P. Mundel, S. J. Shankland, "Podocyte biology and response to injury," *J. Am. Soc. Nephrol.* **13**, 3005–3015 (2002).

65. K. Endlich, W. Kriz, R. Witzgall, "Update in podocyte biology," *Curr. Opin. Nephrol. Hypertens.* **10**, 331–340 (2001).

66. K. Tryggvason, J. Wartiovaara, "Molecular basis of glomerular permselectivity," *Curr. Opin. Nephrol. Hypertens.* **10**, 543–549 (2001).

67. R. Rodewald, M. J. Karnovsky, "Porous substructure of the glomerular slit diaphragm in the rat and mouse," *J. Cell Biol.* **60**, 423–433 (1974).

68. H. P. Erickson, "Size and shape of protein molecules at the nanometer level determined by sedimentation, gel filtration, and electron microscopy," *Biol. Proced. Online* **11**, 32–51 (2009).

69. J. Peti-Peterdi, "Multiphoton imaging of renal tissues *in vitro*," *Am. J. Physiol. Renal Physiol.* **288**, F1079–F1083 (2005).

70. J. C. Jung, A. D. Mehta, E. Aksay, R. Stepnoski, M. J. Schnitzer, "*In vivo* mammalian brain Imaging using one- and two-photon fluorescence microendoscopy," *J. Neurophysiol.* **92**, 3121–3133 (2004).

71. J. Peti-Peterdi, I. Toma, A. Sipos, S. L. Vargas, "Multiphoton imaging of renal regulatory mechanisms," *Physiol.* **24**, 88–96 (2009).

72. A. H. Salmon *et al.*, "Evidence for restriction of fluid and solute movement across the glomerular capillary wall by the subpodocyte space," *Am. J. Physiol. Renal Physiol.* **293**, F1777–F1786 (2007).

73. J. Peti-Peterdi, J. J. Kang, I. Toma, "Activation of the renal renin-angiotensin system in diabetes — new concepts," *Nephrology Dialysis Transplantation* **23**, 3047–3049 (2008)

74. K. W. Dunn, R. M. Sandoval, B. A. Molitoris, "Intravital imaging of the kidney using multiparameter multiphoton microscopy," *Nephron Exp. Nephrol.* **94**, e7–e11 (2003).

75. M. L. Onozato *et al.*, "Optical coherence tomography of human kidney," *J. Urol.* **183**, 2090–2094 (2010).